Effect of strong nonuniformity in grain boundary energy on 3-D grain growth behavior: A phase-field simulation study

Kunok Chang [a,b,d,]*, Long-Qing Chen [b], Carl E. Krill III [c], Nele Moelans [d]

[a] Korea Atomic Energy Research Institute, Daejeon, Republic of Korea
[b] Department of Materials Science and Engineering, The Pennsylvania State University, University Park, PA 16802, USA
[c] Institute of Micro and Nanomaterials, Ulm University, 89081 Ulm, Germany
[d] Department of Materials Engineering, KU Leuven, Kasteelpark Arenberg 44, Box 2450, B-3001 Heverlee, Belgium

ABSTRACT

Large-scale phase-field simulations were performed of the evolution of grain structures with nonuniform grain boundary energy. A novel approach is proposed to determine the average grain boundary dihedral angles between the grain faces along triple and quadruple line junctions from 3-D voxel-based microstructures. We examine the effect of grain boundary energy nonuniformity on the distributions of the grain size, number of faces per grain, and dihedral angles between grain faces. We study the effect of the initial grain size distribution on the evolution toward steady state for both nonuniform and uniform boundary energy systems. The steady-state grain size and number of faces distributions remain uni-modal under all conditions investigated, whereas the dihedral angle distribution is found to become multi-modal when the ratio $R = \sigma_H/\sigma_L$ between high and low grain boundary energies lies in the range of 1.39–1.81. In addition, when $R \approx \sqrt{2}$ a topological transition is observed from a structure with grain faces meeting at triple lines (which themselves terminate in quadruple points) toward one in which the grain faces meet primarily at quadruple line junctions (ending at compact regions of triple junctions or very short triple lines).

© 2016 Elsevier B.V. All rights reserved.

1. Introduction

Grain growth is one of the most common phenomena that occur during materials processing. To predict the macroscopic properties of polycrystalline materials, it is important to understand the evolution of topological characteristics of grain structures during grain growth. Therefore, there has been intensive effort to quantitatively measure and theoretically model such topological characteristics. For instance, analytical 3-D grain size distributions were proposed by Hillert [1] and by Rios and Glicksman [2]. The grain size distributions that arise from grain growth in systems with uniform grain boundary energy were analyzed using the phase-field method [3–5], the Monte Carlo Potts model [6,7], Surface Evolver [8], and the vertex model [9]. Additionally, the effect of the initial grain size distribution on evolution toward the steady-state distribution has been studied for systems with uniform boundary energy [10,11].

Since nonuniformity in grain boundary properties complicates grain growth behavior and its mathematical description, 3-D grain growth under nonuniform boundary energy conditions has been investigated much less frequently by computational methods. Most phase-field grain growth studies with anisotropic grain boundary energy have been performed on 2-D systems [12,13], which is relatively simple and computationally affordable. In 3D, Suwa and colleagues [14] assessed the effect of anisotropy in grain boundary mobility on grain growth kinetics, assuming uniform grain boundary energy. Kim and colleagues [15] incorporated a grain boundary energy database for bcc Fe into a phase-field model to investigate the effect of grain boundary energy anisotropy on grain growth behavior. They measured the average grain size and grain size distribution to quantify the simulated microstructures. In our study, we have measured additional characteristics—two types of dihedral angles and the number of grain faces—to quantify 3-D grain morphologies. Chang and Moelans [16] used phase-field simulations to investigate the effect of nonuniform grain boundary energy on grain growth in 2D; here, a system containing two energy components was considered to be a non-conserved two-phase system, as described by Cahn [17] and Holm et al. [18]. One component was assumed to have the grain boundary energy

* Corresponding author at: Korea Atomic Energy Research Institute, Daejeon, Republic of Korea.

E-mail address: kunokchang@kaeri.re.kr (K. Chang).

σ_H and the other component to have the grain boundary energy σ_L. The simulations performed in Ref. [16] found that when the ratio $R = \sigma_H/\sigma_L$ was larger than or equal to 1.67, the 2-D polycrystal developed a bimodal grain size distribution.

In the present study, we focus on the influence of grain boundary energy nonuniformity on microstructural evolution in 3D. In particular, we vary the ratio R and measure various microstructural characteristics as a function of the degree of nonuniformity, thereby extending the approach of Ref. [16] to 3D to examine the possible appearance of a bimodal grain size distribution during grain growth. We also perform a set of simulations to determine if there is a steady-state distribution when $R > 1.00$.

Additionally, we evaluate the effect of grain boundary energy nonuniformity on the steady-state microstructural characteristics of 3-D grain structures, such as the distributions of grain size, number of faces, and dihedral angles between grain boundaries. A new method is developed to determine the average dihedral angle between grain boundary planes and the dihedral angle between triple junction lines in voxel-based 3-D microstructures. There have been several recent attempts to extract dihedral angles from voxel-based representations of microstructures [16,19–21]. The methods proposed previously are applicable to 2-D structures [16,19], but in 3D, they are limited to the case of two solid particles in a liquid matrix [20]. For example, in Ref. [21], dihedral angles were measured through contour fitting. In space-filling ensembles of grains in 3D, most grain faces are relatively flat and grain connectivity is usually highly complex, which makes it difficult to extend contour fitting to the determination of dihedral angles between grain boundaries meeting at a triple junction line. Furthermore, in 2-D microstructures it is straightforward to determine the dihedral angles between grain boundaries at triple point junctions (or higher-order junctions) [16], but in 3D, the triple line junctions are themselves curved in space (especially when the grain boundary energy is nonuniform), in which case the dihedral angle can depend on position along the triple line junction.

To avoid confusion, we clarify the terminology used in this paper when referring to various types of junctions:

1. Triple/quadruple line junction: a line along which three/four grain faces or grain boundary planes intersect.
2. Triple/quadruple point junction: an intersection point of three/four grains or three/four line junctions.

2. Computational details

2.1. Phase-field model of grain growth

For this investigation, we adopted the multi-order parameter phase-field grain growth model with nonuniform boundary energy of Ref. [16], which is based on the grain growth model with uniform boundary energy that was proposed by Chen and Yang [22], optimized by Active Parameter Tracking (APT) [23]. In this approach, each grain is represented by a set of non-conserved order parameters that are a function of time t and position $\vec{r}$:

$$\eta_1(\vec{r}, t), \eta_2(\vec{r}, t), \ldots, \eta_Q(\vec{r}, t) \tag{1}$$

The temporal and spatial evolution of the order parameters are governed by the time-dependent Ginzburg–Landau equation:

$$\frac{\partial \eta_i}{\partial t} = -L \frac{\delta F}{\delta \eta_i} \tag{2}$$

where

$$F = \int_V \left[\sum_i^Q \left(\frac{\eta_i^4}{4} - \frac{\eta_i^2}{2} \right) + \sum_i^Q \sum_{i \neq j}^Q \theta_{ij} \eta_i^2 \eta_j^2 + \frac{\kappa}{2} \sum_i^Q (\nabla \eta_i)^2 \right] dV \tag{3}$$

The coefficient L in Eq. (2) is a parameter related to the grain boundary mobility, and the coefficient θ_{ij} controls grain boundary nonuniformity. As proposed in Ref. [16], we assume that all order parameters with an even index represent the grains of one of two components and all order parameters with an odd index the grains of the other component. The grains belonging to the two different components are labelled ρ (even index) and τ (odd index) grains. In order to introduce nonuniformity in the grain boundary energy, we use two values for θ_{ij} in Eq. (3). When $i + j$ is an odd number (i.e. the neighboring grains are of a different kind), we assume $\theta_{ij} = \theta_H$; otherwise (i.e. the neighboring grains are of the same kind), $\theta_{ij} = \theta_L$. We define $\theta_H \geqslant \theta_L$ and, therefore, a grain boundary associated with θ_H is a high-energy grain boundary (σ_H, grain boundary energy between ρ-τ grains), and the boundary described by θ_L is a low-energy grain boundary (σ_L, grain boundary energy between ρ-ρ grains or τ-τ grains). κ is the gradient coefficient, which (for a given value of θ_{ij}) determines the width of the diffuse transitions in values of the order parameters at grain boundaries. We assumed $L = \kappa = 1$ in our simulations.

The grain boundary energy ratios considered in this study are listed in Table 1. To measure the grain boundary energies associated with various θ_{ij} values (with $\kappa = 1$), we considered 1-D systems with a single grain boundary and evaluated the grain boundary energy numerically by integration over the boundary profile [24]. The results for specific θ_H and θ_L values are collected in Table 1, and the general dependency of grain boundary energy on θ_{ij} for the considered model is plotted in Fig. 1. We find that the relation

$$\sigma(\theta_{ij}) = 0.384\theta_{ij}^{0.216} - 0.013\theta_{ij}^{-4.33} \tag{4}$$

closely fits the numerically calculated data. The approximate grain boundary width (w_H, w_L in grid points) is also indicated in Table 1 for the considered θ_{ij} values. We counted the number of grid points for which $0.1 < \eta_1 < 0.9$ to evaluate the grain boundary width, and in Fig. 2 we plot profiles of the order parameter across the grain boundary for various values of θ_{ij}.

Additional details concerning the phase-field model can be found in Ref. [16]. The first multi-order parameter phase-field grain growth model was proposed by Chen and Yang [19]. Due to limitations in compute time and memory, the number of order parameters of the original model was well below the number of grains. Since each order parameter corresponded to multiple grains or grain orientations, unphysical grain coalescence occurred whenever two grains having the same order parameter came into contact. To circumvent this problem, Vedantam and Patnaik [23] proposed the APT algorithm, which allows the use of a different order parameter for each grain present in the initial grain structure at relatively low computational cost. Therefore, grain coalescence is avoided entirely. Moreover, since only the active order parameter is solved at each location in the simulation cell, both computational time and memory are saved. Later, an alternative algorithm, the bounding box algorithm, was proposed with the same aim, namely to avoid unphysical grain coalescence and reduce the computational load of the phase field simulation [25]. An advantage of the bounding box algorithm is that it is compatible with a semi-implicit discretization scheme, which permits the use of larger discretized time steps.

In a former study, we used the bounding box algorithm with semi-implicit time-stepping [26]. However, to apply semi-implicit time stepping to a model with inhomogeneous grain boundary properties, one must perform $2n_g$ forward Fourier transforms and n_g backward Fourier transforms, where n_g denotes the number of grains present at a given time step. Since the forward/backward Fourier transformation is computationally highly costly, there is a trade-off between the computational demands of the APT

Table 1
For various values of θ_H and θ_L, the corresponding high (σ_H) and low (σ_L) grain boundary energies and their ratio $R = \sigma_H/\sigma_L$. All grain boundary energies were calculated by numerical integration across interfacial profiles generated by the phase-field model of Section 2.1 with $\kappa = 1$. The grain boundary widths w_H and w_L correspond to the θ_H and θ_L values, respectively, and are given in units of the grid spacing Δx.

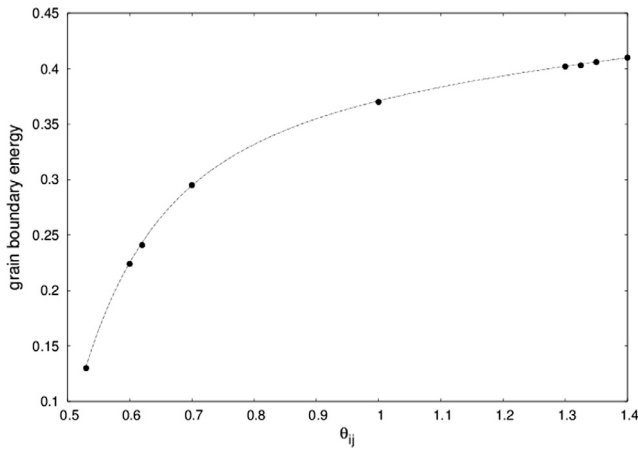| θ_H	θ_L	σ_H	σ_L	w_H	w_L	$R = \sigma_H/\sigma_L$
1.000	1.000	0.370	0.370	4	4	1.00
1.400	0.700	0.410	0.295	3	6	1.39
1.300	0.620	0.402	0.241	3	6	1.67
1.350	0.600	0.406	0.224	3	7	1.81
1.325	0.530	0.403	0.130	3	11	3.10

Fig. 1. The grain boundary energy σ plotted as a function of the parameter θ_{ij} in the free energy function Eq. (3), assuming $\kappa = 1$. Data points (filled circles) were obtained by numerical integration of the free energy across grain boundary profiles in 1D; the dashed curve is a least-squares fit of a power law, yielding Eq. (4).
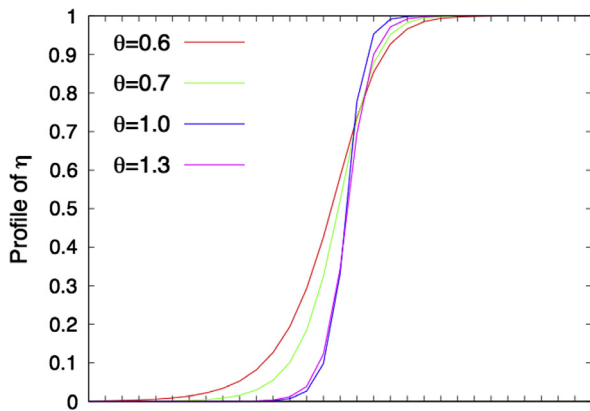

Fig. 2. Plot of the variation of the order parameter η across a 1-D grain boundary for different values of $\theta_{ij} = \theta$. Along the horizontal axis the spacing between adjacent tick marks is Δx.

and bounding box algorithms. For the present study in 3D, we chose the APT algorithm with a simple forward Euler integration scheme,

$$\eta_i(t + \Delta t) \approx \eta_i(t) + \frac{\partial \eta_i}{\partial t}\Delta t, \tag{5}$$

where Δt represents the discretized time step; in all simulations Δt was set to 0.1. Furthermore, for calculation of the Laplacian term in Eq. (3), we need the spatial discretization step size, which we set to $\Delta x = 1.0$ [3].

2.2. Validation for triple junctions

Since the dihedral angles between grain faces meeting at triple and quadruple line junctions are measured in a plane perpendicular to the line junction, it is sufficient to validate the accuracy of the proposed model with 2-D simulations. The 3-grain system considered for validation of dihedral angles is shown in Fig. 3. In this construction, the grain boundary between grains I and III is given the higher energy value σ_H, and the energies of the other two grain boundaries are set to σ_L. Following the example of Refs. [27,28], an additional bulk driving force term of the form $-\beta(3\eta_1^2 + 3\eta_3^2 - 2\eta_1^3 - 2\eta_3^3)$ is added to the free energy density in Eq. (3) for the validation simulations. This additional term is needed to counteract the curvature-driven growth of grain II into grains I and III and thereby obtain a stationary equilibrium boundary configuration in the presence of the triple junction. The value of β is chosen such that the bulk driving force exactly balances out the driving force of curvature for the considered system size and grain boundary energy values. (Practically, this was achieved by incrementally increasing the β value until migration of the curved grain boundary ceases and an equilibrium microstructure like those shown in Fig. 4 is obtained.) Additional details concerning the validation simulations are provided in the supplementary information.

Note that the bulk driving force is not present in the simulations of polycrystalline structures discussed later in the paper. We verified that the bulk driving force had a negligible effect on the dihedral angle by performing simulations with three different system sizes (namely, 400^2, 600^2 and 800^2 grid points), keeping the grain boundary properties the same. Since the grain boundary curvature decreases with increasing system size, a lower value of β is required to achieve equilibrium of a larger system size having the same grain boundary properties. Despite the systematic change in β, the measured triple junction angles were nearly identical in all three cases and close to the angles predicted by Young's law.

To extract triple junction angles from the equilibrium microstructures shown in Fig. 4, we evaluated the quantity d defined by the construction shown in Fig. 3, which enables us to
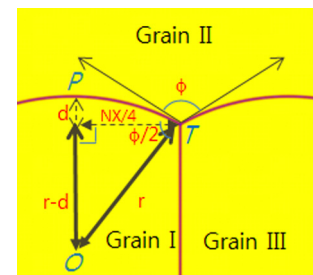

Fig. 3. The equilibrium configuration of three grains meeting at triple junction T, used to validate the accuracy with which dihedral angles between grain faces are reproduced by our phase-field simulation algorithm. The grain boundary energy between grains I and III is assigned to the higher value σ_H, while the energies of the other two grain boundaries are set to the lower value σ_L.
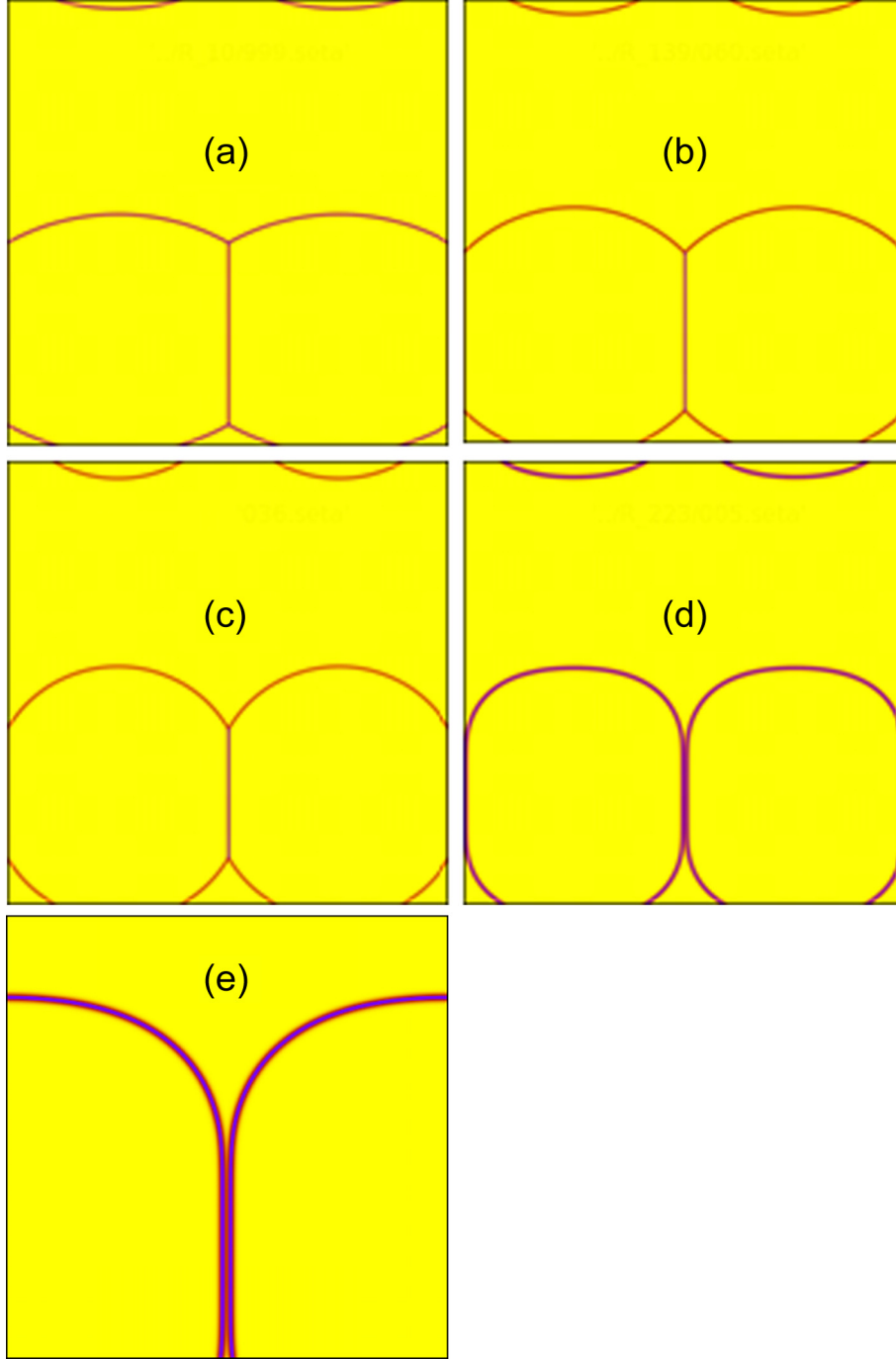
Fig. 4. Equilibrated (a–c) and non-equilibrated (d, e) 3-grain configurations obtained for various grain boundary energy ratios $R = \sigma_H/\sigma_L$: (a) $R = 1.00$, (b) $R = 1.39$, (c) $R = 1.67$ and (d) $R = 2.23$ (for (d), no triple junction was formed, and the boundary between grain I and III is wetted by grain II). (e) Higher-magnification view of the wetted grain boundaries of (d), illustrating penetration of the upper grain into the boundary between the two lower grains. As in Fig. 3, the grain boundary energy between the two lower grains is σ_H, whereas the energy of the boundary between the upper grain and the two lower grains is σ_L. Periodic boundary conditions were applied in both the horizontal and vertical directions.

calculate the radius of curvature r using the relation $r^2 = (r - d)^2 + \frac{(NX)^2}{16}$, with NX the side length of the simulation cell. Finally, we calculated the dihedral angle as $\frac{\phi}{2} = \cos^{-1}\left(\frac{NX/4}{r}\right)$. The center position O in Fig. 3 was determined to maintain $\overline{OT} = \overline{OP}$.

As shown in Fig. 4, we measured the dihedral angle obtained in the phase-field simulations of triple junctions with grain boundary energy ratios $R = \sigma_H/\sigma_L = 1.00$, 1.39, 1.65 and 2.23. Each measured dihedral angle is compared to the angle expected from the

equation for force balance at the triple junction, i.e. Young's law, which yields

$$\phi = 2\cos^{-1}\left(\frac{\sigma_H}{2\sigma_L}\right) = 2\cos^{-1}\left(\frac{R}{2}\right). \tag{6}$$

When $R = 1.00$, the dihedral angle at the triple junction obtained from the simulated system shown in Fig. 4(a) is 122.78°, which is close to the theoretical value of 120° calculated using Eq. (6). When $R = 1.39$, the dihedral angle evaluated from

the simulations is 90.83°, while the theoretical value is 91.95°. When $R = 1.67$, the value obtained from our simulation is 63.60°, whereas the theoretical value from Eq. (6) is 66.77°. For $R = 2.23$, the grain boundary between the two lower grains is entirely wetted (see Fig. 4(d)). The grain boundary region of Fig. 4(d) is shown at higher magnification in Fig. 4(e), where it is clear that the upper grain (grain II in Fig. 3) has penetrated into the grain boundary between the two lower grains. This result is consistent with thermodynamics, which predicts the wetting of a grain boundary when $R > 2.0$ (as the energetic cost of forming two boundaries of energy σ_L is less than the energy of one boundary with σ_H). The discrepancy between the dihedral angle found by simulation and that of theory is thus 2.2%, −1.2% and −4.7% when $R = 1.00$, 1.39 and 1.65, respectively. Therefore, we conclude that the proposed phase-field model reproduces quite accurately the theoretically expected dihedral angles at triple junctions.

2.3. Method to measure dihedral angles in 3D

Here, we describe a novel approach to determining the average dihedral angle between grain boundary planes along a triple or quadruple line junction from 3-D voxel-based microstructure representations. In this method, we first label all voxels in the simulation cell using the label of the maximum order parameter, which means the index of the order parameter having the largest order parameter value. For example, the index value would be 11 if $\eta_1 = 0.1$, $\eta_7 = 0.2$ and $\eta_{11} = 0.9$ at a certain grid point. We explain the method for computing the dihedral angles for the case of a triple line junction, but an analogous approach was followed for quadruple line junctions.

Now, if a given voxel is bordered by two differently labelled voxels that also differ from one another, then we may assume that the given voxel marks the location of a triple line or triple point junction, and we call such a voxel a triple voxel. If more than 5 triple voxels are correlated with the same set of order parameter indices, i.e. have the same neighbor grains, it is considered to be a triple line junction, and the dihedral angles along the line junction are determined. At each (triple) voxel along the triple line, the three dihedral angle components − for instance, the angles between grains p, q, and r in Fig. 5 − can be calculated as follows:

1. For all voxels marking the location of a triple line, the angle at position $\overrightarrow{x}$ (the position of the considered voxel) $\phi_1(\overrightarrow{x})$ is determined as the angle between the two vectors $\nabla(\eta_p(\overrightarrow{x}) - \eta_q(\overrightarrow{x}))$ and $\nabla(\eta_q(\overrightarrow{x}) - \eta_r(\overrightarrow{x}))$, which are vectors perpendicular to the grain boundary between grains p and q
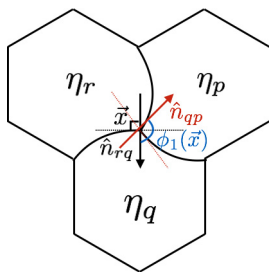

Fig. 5. Triple line junction position $\overrightarrow{x}$ between three grains r, p, and q. We use the vector $\hat{n}_{rq}$ (black arrow) to represent the normal direction to the grain boundary between grains r and q at $\overrightarrow{x}$. Likewise, the vector $\hat{n}_{qp}$ (red arrow) represents the normal direction to the boundary between grains q and p at $\overrightarrow{x}$, and the angle between these two vectors is $\phi_1(\overrightarrow{x})$. We illustrate the grains in 2D for simplicity. (For interpretation of the references to colour in this figure legend, the reader is referred to the web version of this article.)

and the grain boundary between q and r, respectively. The other two angles, $\phi_2(\overrightarrow{x})$ and $\phi_3(\overrightarrow{x})$, are determined in the same manner.

2. When the triple line junction is curved, we find that the measured value of the dihedral angle is dependent on position. Therefore, we calculate the average dihedral angle using the formula described in Eq. (7), where the integral is taken along the entire triple line junction from one endpoint to the other:

$$\Phi_1 = \int_{TL(pqr)} \eta_p^2(\overrightarrow{x})\eta_q^2(\overrightarrow{x})\eta_r^2(\overrightarrow{x})\phi_1(\overrightarrow{x})dl / \int_{TL(pqr)} \eta_p^2(\overrightarrow{x})\eta_q^2(\overrightarrow{x})\eta_r^2(\overrightarrow{x})dl \tag{7}$$

In Eq. (7), the integral path $TL(pqr)$ lies along the triple line junction. We adopt a weighting factor $\eta_p^2(\overrightarrow{x})\eta_q^2(\overrightarrow{x})\eta_r^2(\overrightarrow{x})$ in Eq. (7), which takes on a maximal value along the triple line junction, but which decays rapidly to negligible values inside a grain or grain boundary region.

2.4. Initialization of the grain structure and simulation details

To initiate a polycrystalline structure, 99,999 spherical grains, each with a radius of 4.5 grid points, were randomly distributed over a 3-D simulation domain of $512 \times 512 \times 512$ grid points. Such a large simulation cell was made computationally tractable by the use of 8-node parallel computing employing MPI (Message Passing Interface). 3-D grain structures are shown in Fig. 6 at simulation times of $300\Delta t$ and $8000\Delta t$ for a system with uniform grain boundary energy ($R = 1.00$). We used the state shown in Fig. 6(a) as an initial grain structure for all grain growth simulations, including those with nonuniform boundary energy.

In order to make the examination more rigorous and to study the effect of the initial grain size distribution on the steady-state distribution, we considered two different types of initial grain size distributions: a unimodal and a bimodal distribution. To produce the bimodal grain size distribution, we randomly chose 15,000 grains in the grain structure described above at a simulation time of $300\Delta t$ and merged each of them with an arbitrarily chosen neighboring grain as follows. If, for example η_p is to be merged into η_q, there are two possible cases:

1. If η_p and η_q are both nonzero at a certain position, we take the value of η_q to be $\eta_p + \eta_q$ and set $\eta_p = 0$. If $\eta_p + \eta_q > 1$, then we set $\eta_q = 1$ at that position.
2. If only η_p is nonzero, then we copy the value of η_p to η_q and set $\eta_p = 0$.

We visualize the resulting grain structure in Fig. 7.

In Ref. [29] Chang introduced an error function to quantify the extent to which a particular distribution deviates from Hillert's distribution, which we modified to make the measure independent of the number of bins (nb):

$$Error\_Hillert(A, t) = \sum_{i=1}^{nb} |f_A(i, t) - f_{Hillert}(i, t)| dbin \tag{8}$$

where $f_A(i, t)$ and $f_{Hillert}(i, t)$ are distribution functions at given time t, $nb = 22$ and the bin width dbin set to 0.1 in units of normalized grain diameter (i.e., $D_{max} = nb \cdot dbin \cdot D = 2.2D$, with D denoting the average grain diameter and D_{max} indicating the maximum grain diameter). In this study, we define a grain's diameter D to be the diameter of a sphere of equal volume: $D = \left(\frac{6V}{\pi}\right)^{1/3}$, where V denotes volume of the grain in question. To verify whether the structure has reached steady-state at a particular time step t, we applied an analogous measure to compare the grain size, number of faces or
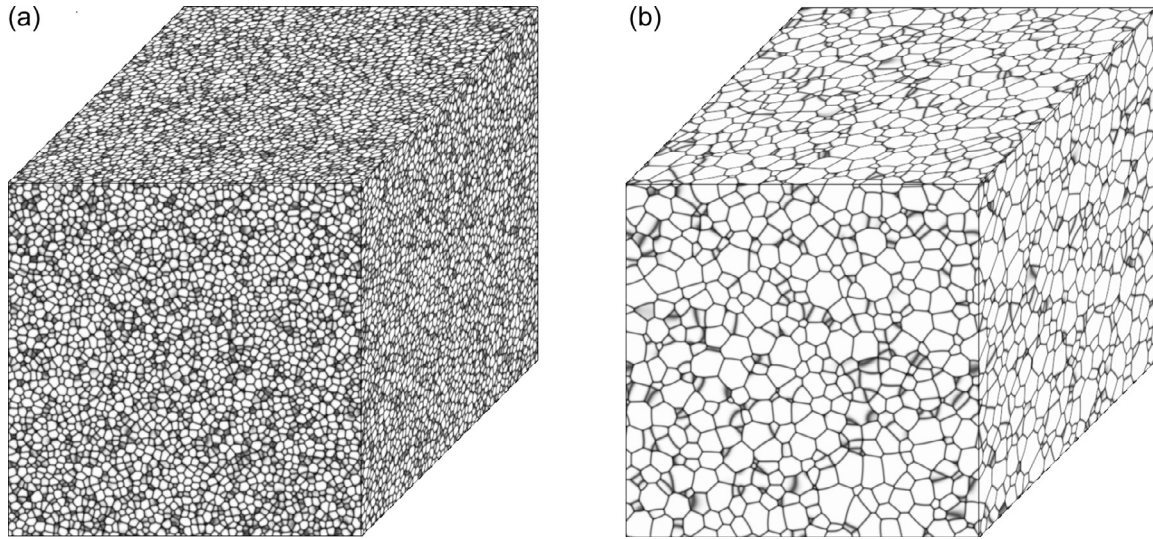
(a) (b)

Fig. 6. 3-D grain structure obtained from a phase-field grain growth simulation performed on a 512^3 simple-cubic grid. The microstructure is visualized by mapping a summation of the squared order parameter values to a gray scale. The grain boundary energy ratio is $R = \frac{\sigma_H}{\sigma_L} = 1.00$. (a) We performed 300 iterations of the simulation to obtain this state (simulation time $300\Delta t$), which still contains all 99,999 grains of the initial configuration. (b) At $8000\Delta t$, 12,091 grains remain in the simulation cell.
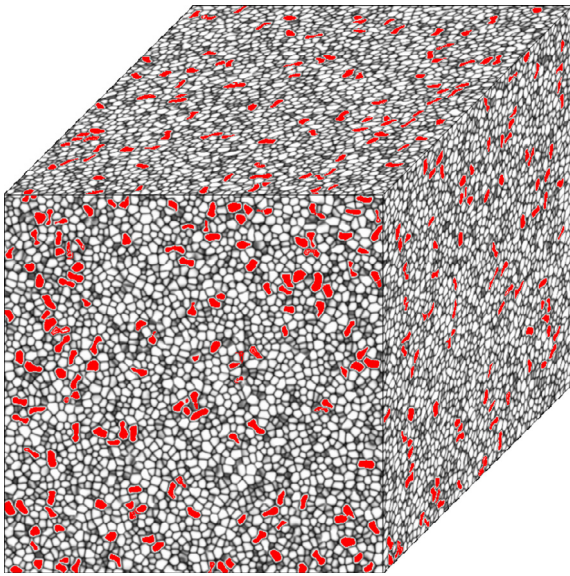
Fig. 7. 3-D simulation cell following the grain-merging process described in the text. The microstructure is visualized by mapping a summation of the squared order parameter values to a gray scale. Merged grains are marked in red. (For interpretation of the references to colour in this figure legend, the reader is referred to the web version of this article.)

dihedral angle distribution obtained at time t with that at time $t + 1000\Delta t$:

$$Error\_Dist(A, t) = \sum_{i=1}^{nb} |f_A(i, t + 1000\Delta t) - f_A(i, t)| dbin \quad (9)$$

We assume that if $Error\_Dist(A, t) \leqslant 0.1$ for all distributions, the structure is evolving in a steady-state manner. For all the considered structures and times, at least 5000 grains disappeared in the considered time intervals of $1000\Delta t$. The structures have thus evolved to a significant extent during these time intervals, and a value $Error\_Dist(A, t) \leqslant 0.1$ is then a reasonable criterion to indicate self-similarity.

2.5. Triple line and quadruple line junction networks

In Fig. 8(a) and (b), the obtained configurations of triple and quadruple voxels are shown for simulations with $R = 1.00$ and 1.81, respectively. We can identify triple/quadruple lines as line-shaped sequences of triple/quadruple voxels; likewise, triple/ quadruple points are identified as localized collections of a few triple/quadruple voxels. Fig. 8(a) then shows that when $R = 1.00$ all grain faces meet at triple line junctions, with the triple lines terminating at quadruple point-shaped junctions. However, Fig. 8(b) shows that when $R = 1.81$, the situation is almost entirely reversed: here, four grain faces meet at line-shaped quadruple junctions, which end at spatially compact regions of triple point junctions and short triple line junctions. More specifically, we find that when $R = 1.00$ or 1.39, all quadruple junctions are point-like, and when $R \geqslant 1.67$, the quadruple junctions tend to become extended lines, and the triple line junctions shorten and reduce to compact regions of triple points. Note that a similar phenomenon was observed in 2D, where we found quadruple junctions to become stable for $R \geqslant \sqrt{2.0}$ and to constitute the major junction type when $R \geqslant \sqrt{3.0}$ [16], in agreement with predictions by Cahn [17] and Holm et al. [18]. The observations gleaned from the 3-D simulations reported above support the occurrence of a similar topological transition in 3D: namely, that quadruple line junctions become stable for $R \geqslant \sqrt{2.0}$. The ratio of the number of triple voxels to quadruple voxels is 52.97 when $R = 1.0$ but only 0.18 when $R = 1.81$.

3. Effect of grain boundary energy nonuniformity on the steady-state distributions of the grain size, number of faces, and dihedral angles between grain faces

The grain structures obtained from the simulations are plotted in Fig. 6(a) and (b) for the grain boundary energy ratio $R = \frac{\sigma_H}{\sigma_L} = 1.00$ and in Fig. 9 for the ratio $R = \frac{\sigma_H}{\sigma_L} = 3.10$.

3.1. Grain size distribution

According to Fig. 10, in the case of a grain boundary energy nonuniformity of $R \geqslant 1.39$, the steady-state grain size distribution
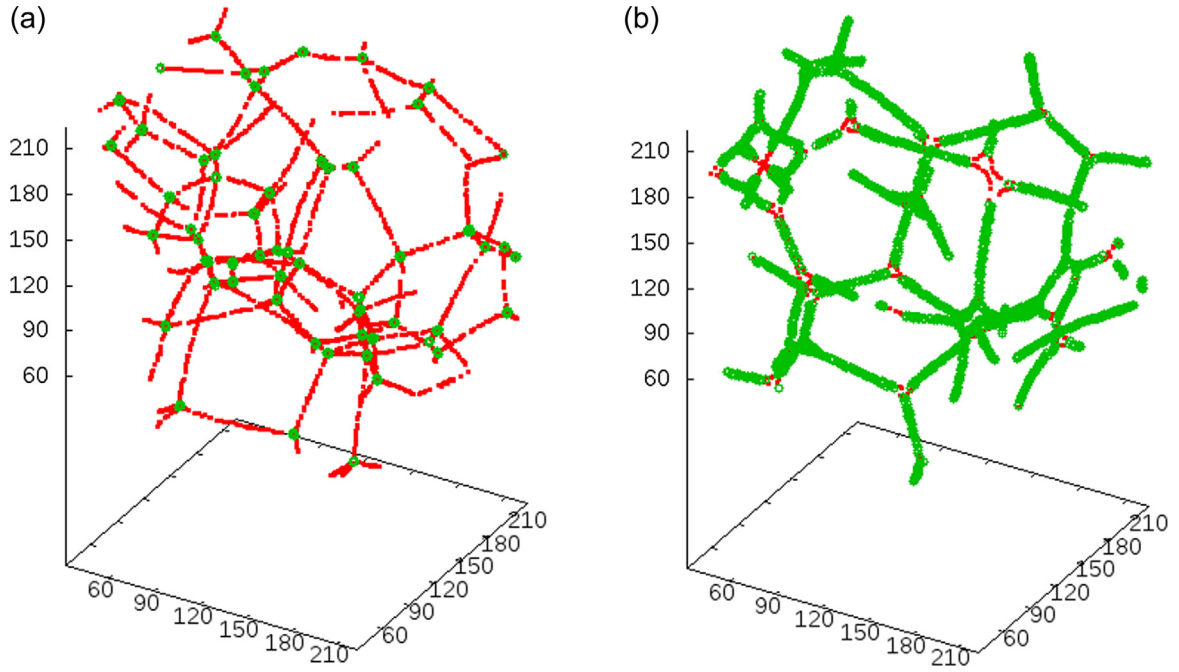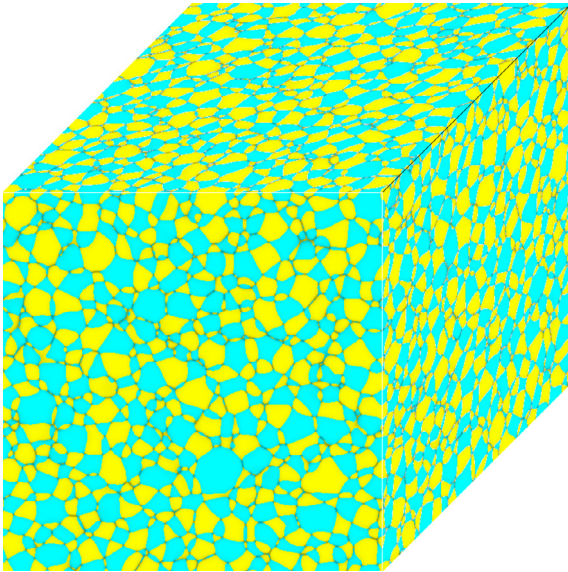
(a)

(b)

Fig. 8. Representation of the positions of triple and quadruple voxels, i.e. all voxels surrounded by 2 or 3 voxels belonging D/D to a different grain for (a) uniform grain boundary energy ($R = 1.00$) and (b) nonuniform grain boundary energy with $R = 1.81$. The red dots indicate triple voxels, and the green dots indicate the locations of quadruple voxels. Between $R = 1.00$ and 1.81 the line junctions of grain boundary planes undergo a transition from only triple line junctions to predominantly quadruple line junctions (only part of the simulation domain is depicted in these figures). (For interpretation of the references to colour in this figure legend, the reader is referred to the web version of this article.)

Fig. 10. The steady-state grain size distributions obtained in the simulations for different grain boundary energy ratios R, plotted against the normalized grain diameter at the indicated times.

Fig. 9. 3-D grain structure obtained from a phase-field grain growth simulation performed on a 512^3 cubic grid. The ρ grains and τ grains are shown in cyan and yellow, respectively. The grain boundary energy ratio is $R = \frac{\sigma_H}{\sigma_L} = 3.10$. At $9000\Delta t$, 13,416 grains are present in the simulation cell. (For interpretation of the references to colour in this figure legend, the reader is referred to the web version of this article.)

is broader than that obtained in the uniform boundary energy case. The diameter of the largest grain for $R = 1.00$ is $2.15D$, with D denoting the average grain diameter, while for $R = 1.39$, the largest grain diameter is $2.40D$, and for $R = 3.10$ it is $2.65D$. In a two-dimensional system, the steady-state grain size distributions are bimodal when $R = 3.10$ [16].
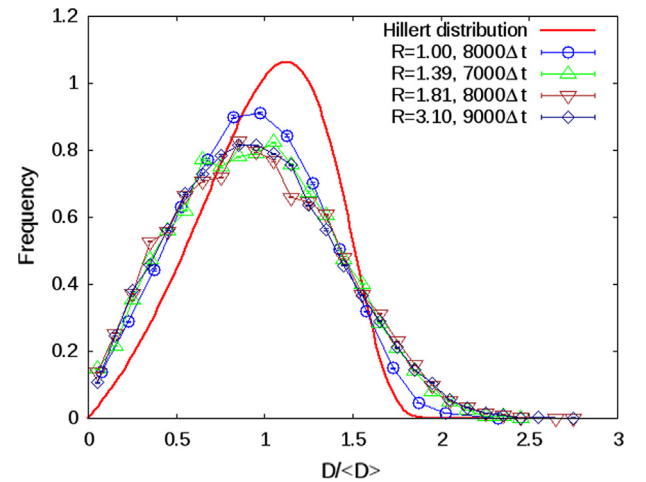
Kim et al. [4] claimed that the steady-state grain size distribution obtained for grain growth with uniform boundary energy converges to Hillert's distribution. On the other hand, Kamachali and Steinbach [5] observed that the grain size distribution is close to Hillert's distribution during a transient regime but that the steady-state distribution is broader than Hillert's distribution [3,5,30,31]. Our results are consistent with Kamachali and Steinbach's work. As shown in Fig. 11, the grain size distribution obtained in this study for $R = 1.00$ is fairly close to Hillert's distribution at the intermediate simulation time $1100\Delta t$; however, at later simulation times ($1900\Delta t$ and beyond) the grain size distribution takes on a steady-state shape that is broader and more symmetric than Hillert's distribution.
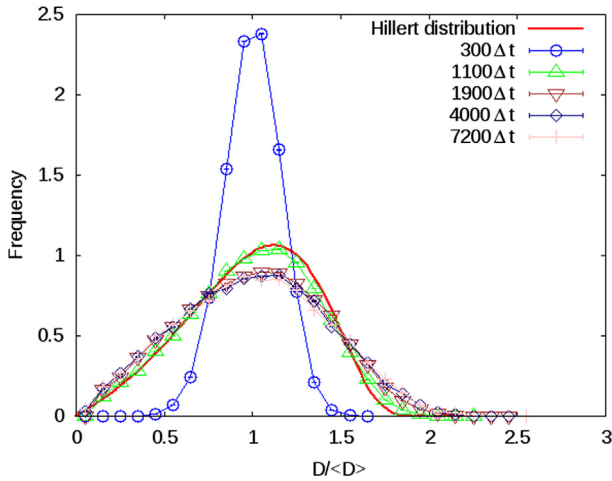
Fig. 11. Evolution of the grain size distribution, plotted as a function of grain diameter normalized by the average value D at the indicated time step. The grain boundary energy ratio for this simulation was $R = \frac{\sigma_H}{\sigma_L} = 1.0$.

Fig. 13. The steady-state distributions of the number of faces for four different grain boundary energy ratios R.

3.3. Dihedral angle distribution

In the case of a homogeneous grain boundary energy ($R = 1.00$), the distribution is sharply peaked at 120°, in agreement with the force balance equation. As we have shown in Ref. [16], in 2-D systems the dihedral angle distribution possesses a clearly bimodal shape when $R = 1.39$, and the distribution has a single peak at 90° for $R \geqslant 1.67$. In this study, we find that in 3-D systems a bimodal distribution of the average dihedral angle at triple lines develops when $1.39 \leqslant R \leqslant 1.81$, as shown in Fig. 14(b)–(d). According to Young's law, dihedral angles of 91.95° and 134.03° should be obtained when $R = 1.39$. In the simulated microstructures, however, the distribution of the triple line junction dihedral angles is peaked around 60° and 150° for $R = 1.39$ (Fig. 14(b)), and higher values of R lead only to small shifts in these peak positions, with a concomitant reduction in the relative fraction of grain boundaries meeting at triple lines versus quadruple lines (Fig. 13(b–d)). Such behavior is highly reminiscent of the findings reported in Ref. [16] for 2-D systems with $\sqrt{2} \leqslant R \leqslant \sqrt{3}$, for which the contribution from triple junctions was found to manifest two peaks, one around 70–80° and another around 150°; in this case, it could be shown that the deviation from theoretically expected angles arose as a result of geometrical restrictions imposed by the surrounding network of grain boundaries. In the present work, we have shown that our phase-field model will reproduce dihedral angles accurately if the surrounding network allows for it. Therefore, we conclude that, also in 3D, deviations in dihedral angles from expected equilibrium values can arise as the result of topological restrictions imposed by the surrounding grain boundary network. Moreover, the distribution of average dihedral angles at quadruple lines is peaked at 90° for $R \geqslant 1.39$, which again is consistent with the 2-D microstructures reported in Ref. [16].

4. Role of the initial grain size distribution on the steady-state grain size distribution

To study the effect of the initial grain size distribution on the steady-state distributions, we carried out simulations starting from an initial grain structure with a bimodal grain size distribution. This initial configuration was obtained by merging grains in a classical grain structure with a unimodal grain size distribution, as described in Section 2.4 (see Fig. 7). Simulations were performed starting from the bimodal structure with merged grains, and the evolution of the grain size distribution is plotted in Figs. 15 and

In our studies, we assumed that a grain size distribution deviates from Hillert's distribution when $Error\_Hillert(A, t) > 0.1$ (number of bins equal to 20 and a maximum grain diameter of $2.0D$ considered in this evaluation). For example, $Error\_Hillert(A, t = 7200\Delta t)$ has the value 0.25 in Fig. 11. We plot the evolution of $Error\_Hillert(A, t)$ as grain growth proceeds in Fig. 12: $Error\_Hillert(A, t)$ drops significantly at $t = 1100\Delta t$, but at later times it takes on a constant value of approximately $Error\_Hillert(A, t) = 0.22$.

3.2. Number of faces distribution

For 2-D systems, we showed that the number of faces peaks at 6 for $R = 1.00$ and 3 in nonuniform boundary energy cases with $R \geqslant 1.39$ [16]. For 3-D systems, on the other hand, as shown in Fig. 13, the steady-state distribution of the number of faces broadens as the ratio of the grain boundary energies R increases. The position of the peak of the distribution, however, remains at $f = 11$ (number of faces per grain) for all R values that we considered. In previous studies [3,5], it was also found that the distribution of the number of faces peaks at $f = 10-11$, and the frequency for $f = 25$ was approximately 0.008 for grain growth with uniform boundary energy in 3-D. The distribution shown in Fig. 13 for $R = 1.00$ is thus consistent with previous observations.
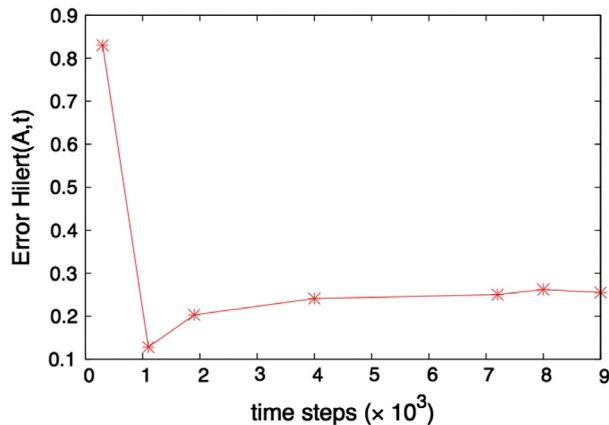

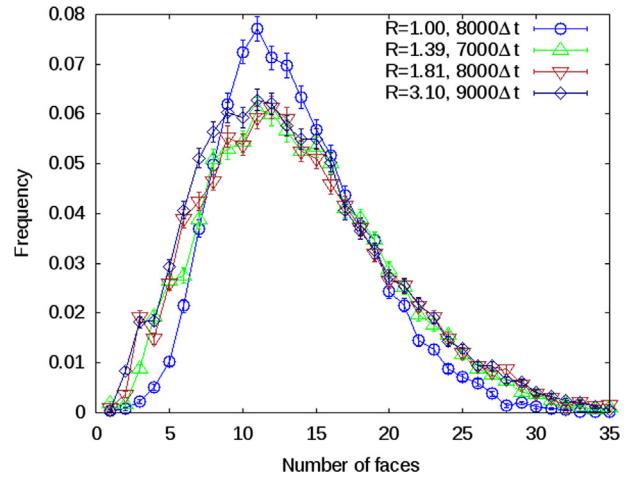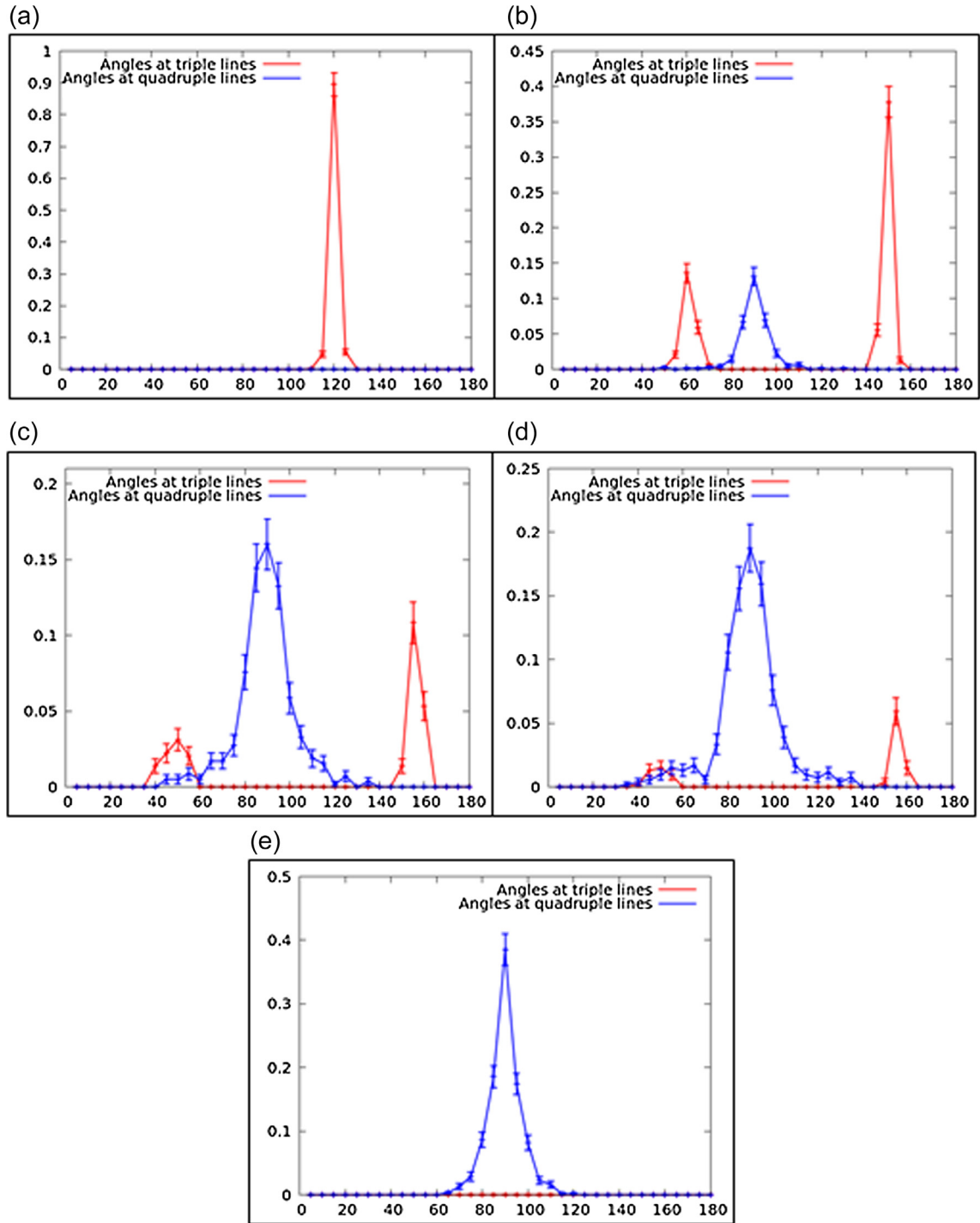**Fig. 12.** Plot of $Error\_Hillert(A, t)$ for the grain size distributions in Fig. 11 as a function of time.

Fig. 14. The steady-state distributions of average dihedral angles at triple line junctions (red) and quadruple line junctions (blue) measured for the various grain boundary energy ratios R investigated in the 3-D simulations: (a) $R = 1.00$, (b) $R = 1.39$, (c) $R = 1.67$, (d) $R = 1.81$ and (e) $R = 3.10$. (For interpretation of the references to colour in this figure legend, the reader is referred to the web version of this article.)

16 for $R = 1.00$ and $R = 3.10$, respectively. In the uniform boundary energy case, the grain size distributions remain bimodal until $1000\Delta t$ (Fig. 15). At $2000\Delta t$, the left peak becomes a plateau and the right peak rises higher than the left peak. This behavior is consistent with smaller grains being eliminated preferentially due to their higher curvature, resulting in the overall distribution becoming unimodal. At $5200\Delta t$, the grain size distribution is quite close to Hillert's distribution ($Error\_Hillert(A, t) = 0.072$), just as when

starting from a singly peaked initial grain size distribution. Finally, the simulation converges to the same steady-state grain size distribution as in Fig. 11. We evaluated the $Error\_Dist$ function between the grain size distributions in Fig. 11 (at $7200\Delta t$) and Fig. 15 (at $8000\Delta t$), and the value is 0.099. Therefore, we conclude that the initial grain size distribution did not notably affect the steady-state grain size distribution when $R = 1.00$. For the system with $R = 3.10$, we also found that the initial bimodal grain size distribu-
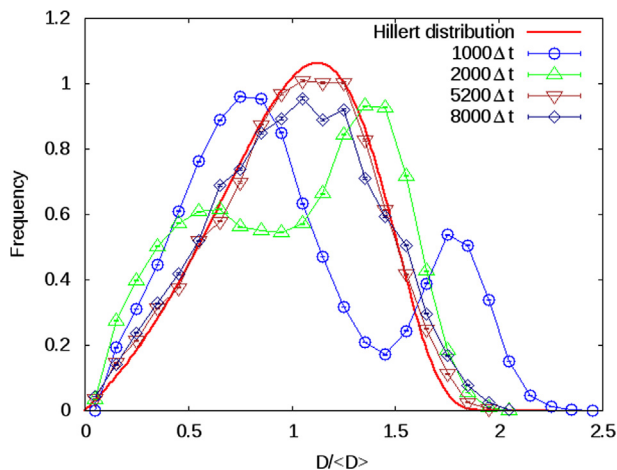
Fig. 15. Frequency plotted against the grain diameter normalized by its average value D at the indicated time step. The initial grain size distribution is bimodal. The grain boundary energy ratio was $R = \frac{\sigma_H}{\sigma_L} = 1.00$ for this simulation.
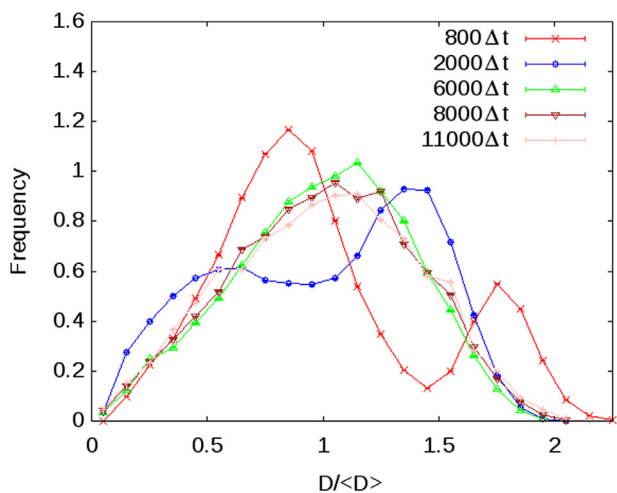

Fig. 16. Frequency plotted against the grain diameter normalized by its average value D at the indicated time step. The initial grain size distribution is bimodal. The grain boundary energy ratio was $R = \frac{\sigma_H}{\sigma_L} = 3.10$ for this simulation.

tion evolves toward an invariant unimodal grain size distribution, which is broader and more symmetric than Hillert's distribution (Fig. 16).

5. Conclusions

Large-scale, 3-D phase-field grain growth simulations were performed for polycrystalline materials containing equal fractions of high (σ_H) and low (σ_L) grain boundary energies by implementing a parallel computing scheme. When the ratio $R = \sigma_H/\sigma_L$ is set to unity, the steady-state grain size distribution is broader and more symmetric than Hillert's distribution, regardless of whether the initial grain size distribution is singly peaked or bimodal. For a short duration within a transient regime, the distribution is fairly close to Hillert's distribution for both unimodal and bimodal initial size distributions. In the case of nonuniform grain boundary energy ($R > 1.00$), the steady-state grain diameter distribution is broader than in the uniform boundary energy case. The distribution of the number of grain faces is also broader than for grain growth with uniform boundary energy, although the peak value $f = 11$ is invariant. In addition, we observed a topological transition at

$R \approx \sqrt{2.0}$ from grain boundary planes intersecting at triple line junctions, which themselves connect quadruple point junctions, to grain boundary planes intersecting predominantly at quadruple line junctions, which terminate in compact regions of triple junctions. This topological transition is similar to the appearance of stable quadruple junctions in 2D when $R \geqslant \sqrt{2.0}$. The distribution of the dihedral angle between grain boundary planes at (triple and quadruple) line junctions peaks at 120° for $R = 1.00$, becomes bimodal or multi-modal for $R = 1.39$, 1.67 and 1.81, and has a single peak at 90° for $R = 3.10$. The growing peak at 90° with increasing value of R can be related to the increasing stability of quadruple line junctions.

Appendix A. Supplementary material

Supplementary data associated with this article can be found, in the online version, at http://dx.doi.org/10.1016/j.commatsci.2016.10.027.

References

[1] M. Hillert, On the theory of normal and abnormal grain growth, Acta Metall. 13 (1965) 227.
[2] P.R. Rios, M.E. Glicksman, Self-similar evolution of network structures, Acta Mater. 54 (2006) 1041.
[3] C.E. Krill III, L.Q. Chen, Computer simulation of 3-D grain growth using a phase-field model, Acta Mater. 50 (2002) 3057.
[4] S.G. Kim, D.I. Kim, W.T. Kim, Y.B. Park, Computer simulations of two-dimensional and three-dimensional ideal grain growth, Phys. Rev. E 74 (2006) 061605.
[5] R.D. Kamachali, I. Steinbach, 3-D phase-field simulation of grain growth; topological analysis versus mean-field approximations, Acta Mater. 60 (2012) 2719.
[6] D. Zollner, P. Streitenberger, Three-dimensional normal grain growth: Monte Carlo Potts model simulation and analytical mean field theory, Scripta Mater. 54 (2006) 1697.
[7] M.P. Anderson, G.S. Grest, D.J. Srolovitz, Computer simulation of normal grain growth in three dimensions, Phil. Mag. B 59 (1989) 293.
[8] F. Wakai, N. Enomoto, H. Ogawa, Three-dimensional microstructural evolution in ideal grain growth – general statistics, Acta Mater. 48 (2000) 1297.
[9] K. Fuchizaki, T. Kusaba, K. Kawasaki, Computer modelling of three-dimensional cellular pattern growth, Phil. Mag. B 71 (1995) 333.
[10] W.E. Benson, J.A. Wert, The effect of initial grain size distribution on abnormal grain growth in single-phase materials, Acta Mater. 56 (1998) 5323.
[11] K. Matsuura, Y. Itoh, Analysis of the effect of grain size distribution on grain growth by computer simulation, ISIJ Int. 31 (1991) 366.
[12] A. Kazaryan, Y. Wang, S.A. Dregia, B.R. Patton, Generalized phase-field model for computer simulation of grain growth in anisotropic systems, Phys. Rev. B 61 (2000) 14275.
[13] A. Kazaryan, Y. Wang, S.A. Dregia, B.R. Patton, Grain growth in anisotropic systems: comparison of effects of energy and mobility, Acta Mater. 50 (2002) 2491.
[14] Y. Suwa, Y. Saito, H. Onodera, Three-dimensional phase field simulation of the effect of anisotropy in grain-boundary mobility on growth kinetics and morphology of grain structure, Comp. Mater. Sci. 40 (2007) 40.
[15] H.K. Kim, S.G. Kim, W. Dong, I. Steincach, B.J. Lee, Phase-field modeling for 3D grain growth based on a grain boundary energy database, Model. Simul. Mater. Sci. Eng. 22 (2014) 034004.
[16] K. Chang, N. Moelans, Effect of grain boundary energy anisotropy on highly textured grain structures studied by phase-field simulations, Acta Mater. 64 (2014) 443.

[17] J.W. Cahn, Stability, microstructural evolution, grain growth, and coarsening in a two-dimensional two-phase microstructure, Acta Metall. 39 (1991) 2189.

[18] E.A. Holm, D.J. Srolovitz, J.W. Cahn, Microstructural evolution in two-dimensional two-phase polycrystals, Acta Metall. 41 (1993) 1119.

[19] G.J. Nelson, K.N. Grew, J.R. Izzo Jr., J.J. Lombardo, W.M. Harris, A. Faes, A. Hessler-Wyser, J.V. Herle, S. Wang, Y.S. Chu, A.V. Vilkar, W.K.S. Chiu, Three-dimensional microstructural changes in the Ni-YSZ solid oxide fuel cell anode during operation, Acta Mater. 60 (2012) 3491.

[20] H. Ravash, E. Specht, J. Vleugels, N. Moelans, 3-D phase-field situation and characterization of microstructure evolution during Liquid Phase Sintering, Adv. Sci. Technol. 87 (2014) 132.

[21] W. Guo, R. Spatschek, I. Steinbach, An analytical study of the static state of multi-junctions in a multi-phase field model, Physica D 240 (2011) 382.

[22] L.Q. Chen, W. Yang, Computer simulation of the domain dynamics of a quenched system with a large number of non conserved order parameters: the grain-growth kinetics, Phys. Rev. B 50 (1994) 15752.

[23] S. Vedantam, B.S.V. Patnaik, Efficient numerical algorithm for multiphase field simulations, Phys. Rev. E 73 (2006) 016703.

[24] N. Moelans, B. Blanpain, P. Wollants, A phase field model for the simulation of grain growth in materials containing finely dispersed incoherent second-phase particles, Acta Mater. 53 (2005) 1771.

[25] L. Vanherpe, N. Moelans, B. Blanpain, S. Vandewalle, Bounding box framework for efficient phase field simulation of grain growth in anisotropic systems, Comp. Mater. Sci. 50 (2011) 2221.

[26] L.Q. Chen, J. Shen, Applications of semi-implicit Fourier-spectral method to phase field equations, Comp. Phys. Commun. 108 (1998) 148.

[27] K. Chang, N. Moelans, Phase-field simulations of the interaction between a grain boundary and an evolving second-phase particle, Phil. Mag. Lett. 95 (2015) 202.

[28] B. Saswata, T.W. Heo, K. Chang, L.Q. Chen, A phase-field model of stress effect on grain boundary migration, Model. Simul. Mater. Sci. Eng. 19 (2011) 035002.

[29] K. Chang, Quantitative evaluation of topological measures from grain structures generated by large-scale phase-field simulations of grain growth PhD Thesis, The Pennsylvania State University, 2011 (Chapter 3).

[30] D. Zollner, P. Streitenberger, Three-dimensional normal grain growth: Monte Carlo Potts model simulation and analytical mean field theory, Scripta Mater. 54 (2006) 1697.

[31] F. Wakai, N. Enomoto, H. Ogawa, Three-dimensional microstructural evolution in ideal grain growth – general statistics, Acta Mater. 48 (2000) 1297.